JACS Au
AN OPEN ACCESS JOURNAL OF THE AMERICAN CHEMICAL SOCIETY

pubs.acs.org/jacsau
Article

Targeting GDP-Dissociation Inhibitor Beta (GDI2) with a Benzo[*a*]quinolizidine Library to Induce Paraptosis for Cancer Therapy

Yong Sun,[▽] Hongbo Zheng,[▽] Lilin Qian, Yue Liu, Deyu Zhu, Zejun Xu, Wenqiang Chang, Jianwei Xu, Lei Wang, Bin Sun, Lichuan Gu, Huiqing Yuan, and Hongxiang Lou*

Cite This: *JACS Au* 2023, 3, 2749−2762

ABSTRACT: Inducing paraptosis, a nonapoptotic form of cell death, has great therapeutic potential in cancer therapy, especially for drug-resistant tumors. However, the specific molecular target(s) that trigger paraptosis have not yet been deciphered yet. Herein, by using activity-based protein profiling, we identified the GDP-dissociation inhibitor beta (GDI2) as a manipulable target for inducing paraptosis and uncovered benzo[*a*]-quinolizidine BQZ-485 as a potent inhibitor of GDI2 through the interaction with Tyr245. Comprehensive target validation revealed that BQZ-485 disrupts the intrinsic GDI2-Rab1A interaction, thereby abolishing vesicular transport from the endoplasmic reticulum (ER) to the Golgi apparatus and initiating subsequent paraptosis events including ER dilation and fusion, ER stress, the unfolded protein response, and cytoplasmic vacuolization. Based on the structure of BQZ-485, we created a small benzo[*a*]quinolizidine library by click chemistry and discovered more potent GDI2 inhibitors using a NanoLuc-based screening platform. Leveraging the engagement of BQZ-485 with GDI2, we developed a selective GDI2 degrader. The optimized inhibitor (+)-**37** and degrader **21** described in this study exhibited excellent *in vivo* antitumor activity in two GDI2-overexpressing pancreatic xenograft models, including an AsPc-1 solid tumor model and a transplanted human PDAC tumor model. Altogether, our findings provide a promising strategy for targeting GDI2 for paraptosis in the treatment of pancreatic cancers, and these lead compounds could be further optimized to be effective chemotherapeutics.

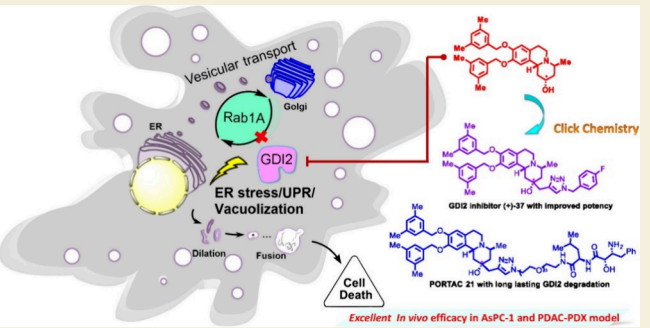

KEYWORDS: *alkaloids, paraptosis, target identification, GDI2 inhibitors, benzo[a]quinolizidine library, click chemistry, cancer therapy*

INTRODUCTION

Targeting noncanonical programmed cell death pathways has been found to have great therapeutic potential for overcoming resistance to chemotherapy for cancer treatment, including in various carcinomas (liver, renal, breast, prostate, colon, gastric, and pituitary cancers) and hematologic malignancies (leukemia and multiple myeloma).[1−5] For example, RIPK inhibitors for necroptosis, GPX4 inhibitors for ferroptosis, and GSDM agonists for pyroptosis have been developed for bypassing drug resistance.[6−10]

Paraptosis is an underexplored form of nonapoptotic programmed cell death that can be targeted for new cancer therapies. It is characterized by extensive vacuolization derived from the dilation of the endoplasmic reticulum (ER) and/or mitochondria.[11] Unlike caspase-dependent apoptosis, paraptosis is associated with different mechanisms that involve the activation of mitogen-activated protein kinases (MAPKs) such as JNKs, MEK-2, and p38. It is often accompanied by disruption of ion homeostasis, such as Ca^{2+} and K^{+}, and disruption of redox homeostasis. In addition, impaired proteostasis and the accumulation of misfolded/unfolded proteins are also commonly observed in paraptosis.[12,13] Over the past few decades, many natural products and synthetic molecules (Figure S1A) have been developed as potent paraptosis inducers, offering potential therapies for various cancers.[12−16] For example, there is evidence that bromocriptine promotes tumor ablation in patients with prolactin-secreting pituitary adenomas by inducing paraptosis through activation of the PKCδ, ERK1/2, and p38 pathways.[17,18] Promising molecules such as WIN55,212-2, VER155008, and Nutlin-3 have shown therapeutic potential in overcoming

Received: May 6, 2023
Revised: September 11, 2023
Accepted: September 12, 2023
Published: September 26, 2023

https://doi.org/10.1021/jacsau.3c00228
JACS Au 2023, 3, 2749−2762

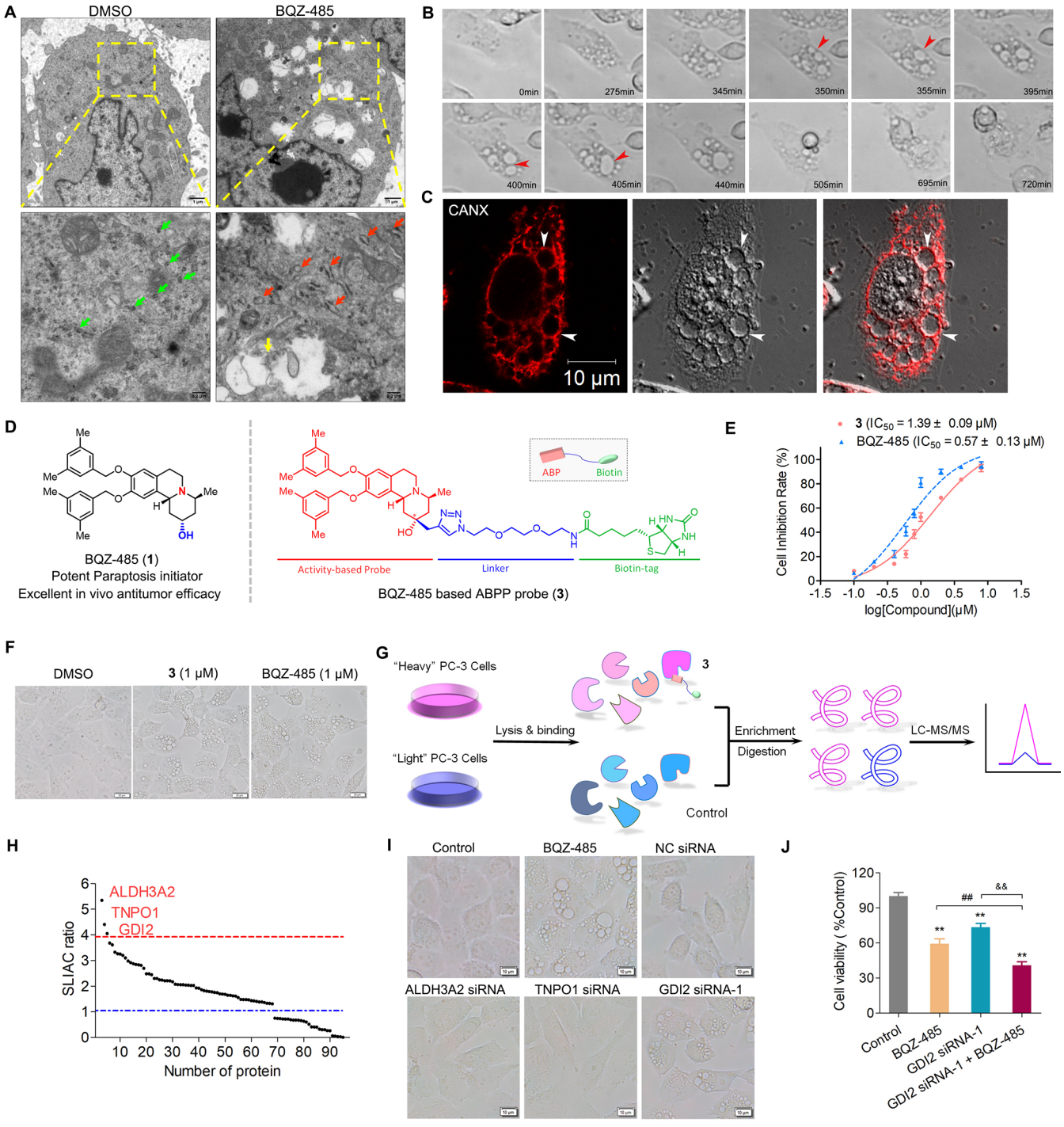

Figure 1. Identification of GDI2 as the molecular target of BQZ-485 for inducing paraptosis. (A) TEM images of the ultrastructure of PC-3 cells treated with vehicle or BQZ-485 (1 μM, 8 h). Green, normal ER lumens; red, dilated ER lumens; yellow, fusing vacuoles. Scale bars: 1 and 0.2 μm. (B) Time-lapse images of BQZ-485 triggered vacuolization in PC-3 cells captured by phase-contrast microscopy (1 μM, 0−720 min). (C) Representative immunofluorescence images for ER markers CANX in BQZ-485 (1 μM, 8 h) treated PC-3 cells. Scale bars: 10 μm. (D) Chemical structure of BQZ-485 (**1**) and BQZ-485-based ABPP probe (**3**). (E) Antiproliferative potencies of BQZ-485 and the biotinylated-based probe (**3**) in PC-3 cells (0.1−10 μM, 48 h). (F) Representative vacuolization images of BQZ-485 and probe **3** treated PC-3 cells (1 μM, 8 h) and DMSO control; scale bars: 20 μm. (G) Schematic view of the ABPP-SILAC strategy to identify the molecular targets of BQZ-485. (H) SILAC ratio plot of the total protein identified by BQZ-485 probe **3** in PC-3 cells. Three *top hits* beyond 4.0 threshold are highlighted. (I) Knockdown of GDI2, ALDHA3A2, or TNOP1 by siRNA in PC-3 cells and corresponding cytoplasmic vacuolization responses. Scale bars: 10 μm. (J) PC-3 cell viability after treatment with GDI2 siRNA, BQZ-485 (1 μM, 48 h), or the combination of both.

apoptosis resistance in mantle cell lymphoma (MCL), anaplastic thyroid carcinoma (ATC), and breast cancer (MDA-MB-435s) cells by inducing paraptosis.[19,20] Moreover, organometallic complexes, especially copper complexes, have also been found to force cancer cells into paraptotic death.[16,21] However, despite the great potential of the induction of

https://doi.org/10.1021/jacsau.3c00228
JACS Au 2023, 3, 2749−2762

paraptosis for the development of new tumor therapies, the molecular target driving this process has yet to be deciphered, highlighting the importance of identifying the crucial target of paraptosis.

We have made significant efforts to search for potent paraptosis inducers,[22−24] and benzo[*a*]quinolizidine BQZ-485 (**1**) stood out as a well-defined paraptosis initiator with excellent tumoricidal activity (Figure 1A,D). To understand the underlying molecular basis of paraptosis and to develop more potent chemotherapeutics, it is crucial to elucidate the unknown molecular target of BQZ-485. The most distinctive phenotype of paraptosis initiated by BQZ-485 is cytoplasmic vacuolization from the dilated ER lumens. This suggests that BQZ-485 targets ER membrane proteins—particularly a component of the vesicular transport system—to disrupt intrinsic membrane homeostasis and induce persistent ER stress. Of the proteins that modulate membrane trafficking processes, Ras-like proteins in the brain (RabGTPases or Rabs) serve as the central coordinators for identifying the cargo delivery destination,[25,26] and they play an important role in tumorigenesis.[27] Thus, we proposed that the functional loss of Rabs may lead to prominent membrane disorders and result in paraptosis-like vacuolization and cell death. Meanwhile, targeting Rab effectors, for example, GDP exchange factors (GEFs), GTPase-activating proteins (GAPs), and GDP-dissociation inhibitors (GDIs),[28] interfe res with the retrieval and reload of Rabs, which, in turn, disrupts intrinsic vesicular trafficking and facilitates tumor cell death.[29,30] Recent research has shown an increasing interest in developing new cancer therapy by targeting the Rab signaling pathway[31−34] and indicated that targeting Rab and its effectors offers opportunities to selectively eliminate tumor cells due to their heavy protein synthesis burden and exuberant vesicle transport.[35,36] However, neither inhibitors that can directly interfere with Rabs nor those that can disrupt Rab interactions with its accessory proteins have been identified thus far,[37] and the potential of targeting the Rab signaling pathway to induce paraptosis has not been investigated.

In this study, we identified GDP-dissociation inhibitor beta (GDI2) as a crucial target for promoting paraptosis by using an activity-based protein profiling (ABPP) strategy and discovered BQZ-485 as a potent GDI2 inhibitor. Comprehensive target validation confirmed that GDI2 is a *bona fide* molecular target of BQZ-485 and that its inhibition by BQZ-485 is capable of eliciting paraptotic cell death in tumors. Further modification of our initial structure led to improved GDI2 inhibitors as well as selective proteolysis targeting chimeras (PROTAC) to degrade GDI2. Furthermore, optimized inhibitor (+)-**37** and degrader **21** exhibited excellent *in vivo* antitumor activity in the GDI2-overexpressing pancreatic xenograft models, providing clear evidence that targeting GDI2 is a promising strategy for cancer therapy.

RESULTS AND DISCUSSION

Identification of GDI2 as the Molecular Target of BQZ-485 for Inducing Paraptosis

We initially investigated the formation of vacuoles induced by BQZ-485 and established its potential target as a crucial protein for maintaining ER membrane homeostasis/permeability. TEM ultrastructure analysis indicated that the vacuoles originated from the fusion of dilated ER lumens, as the vacuoles are enclosed by a monolayer membrane with visible contents and some of them are decorated with ribosomes (Figure 1A). In addition, the dilation of the ER lumen and consecutive fusion events occurred throughout the cell, while other organelles were unaffected (white arrow, Figure S1B). The dynamic process of catastrophic vacuolization in a specific cell was recorded by phase-contrast time-lapse images: numerous small vesicles appeared in the early stage, then coalesced to form larger vacuoles, and eventually triggered cell bursting and the scattering of cell debris (Figure 1B). Immunofluorescence labeling of CANX, a prominent ER-resident chaperone, perfectly overlapped with the membranes of the vacuoles in confocal micrographs (white arrow, Figure 1C), confirming that these intracellular vacuoles were derived from the ER rather than other possible organelles (e.g., early/late endosomes (Rab5/Rab7), mitochondria (TOM20), lysosomes (Lamp2), and autophagosomes (LC3); Figure S1C).

To unravel the molecular target of BQZ-485, we developed an efficient ABPP probe[38−41] based on BQZ-485, which enabled us to uncover its interacting proteins. Among the modified structures, intermediate **2** (Figure S1D) with propargylation at the C_2 position stood out as having comparable activity to BQZ-485, notably because the stereochemistry of the C_2-hydroxyl pharmacophore is preserved. From this structure, we successfully prepared BQZ-485-biotin conjugate **3** via click chemistry (CuAAC), and the ABPP probe **3** was found to exhibit potent antitumor activity and induce vacuolization, which is consistent with the phenotypes obtained after BQZ-485 treatment (Figure 1D−F).

For profiling proteins that directly interact with BQZ-485, stable isotope labeling by amino acids in cell culture (SILAC)-based quantitative proteomic analysis[42,43] was performed in combination with BQZ-485 probe **3**. PC-3 cells were cultured for over 10 passages in "light" (normal) and "heavy" ($[^{13}C_6,^{15}N_4]$ L-arginine and $[^{13}C_6,^{15}N_2]$ L-lysine) SILAC media, respectively. Cells were then lysed, and the "heavy" proteomes were treated with 10 μM biotinylated probe **3**. The light proteomes and probe-labeled heavy proteomes were mixed (1:1) and then subject to streptavidin bead enrichment, on-bead tryptic digestion, and, finally, LC−MS/MS analysis for protein identification and quantification (Figure 1G). Then, the proteins that had been captured by BQZ-485 probe **3** were identified and ranked based on their SILAC ratio (heavy/light) (Figure 1H and Table S1). We set a threshold of 4.0 for the normalized SILAC ratio for top hits, and three proteins—ALDH3A2 (aldehyde dehydrogenase enzyme), TNPO1 (nuclear transport receptor), and GDI2 (Rab effector for regulating vesicular transport)—were discovered as potential targets of BQZ-485 for inducing paraptosis.

We next proceeded to knock down the three candidate proteins in PC-3 cells using siRNA and checked the resulting phenotype and lethality (Figure 1I and Figure S2A). As expected, our results show that the depletion of the nonmembrane proteins ALDH3A2 and TNPO1 did not cause paraptotic cell death. However, silencing GDI2 with two different siRNA sequences resulted in extensive cellular vacuolization and decreased cell viability, which is similar to the effects of BQZ-485 treatment (Figure S2B,C). The dose-dependent effectiveness of GDI2-siRNA was evidenced by a simultaneous decrease in both GDI2 expression and cell proliferation (Figures S2D,E), confirming the critical role of GDI2 in inducing paraptotic cell death. Notably, GDI2-knockdown combined with BQZ-485 treatment produced a

https://doi.org/10.1021/jacsau.3c00228
JACS Au 2023, 3, 2749−2762

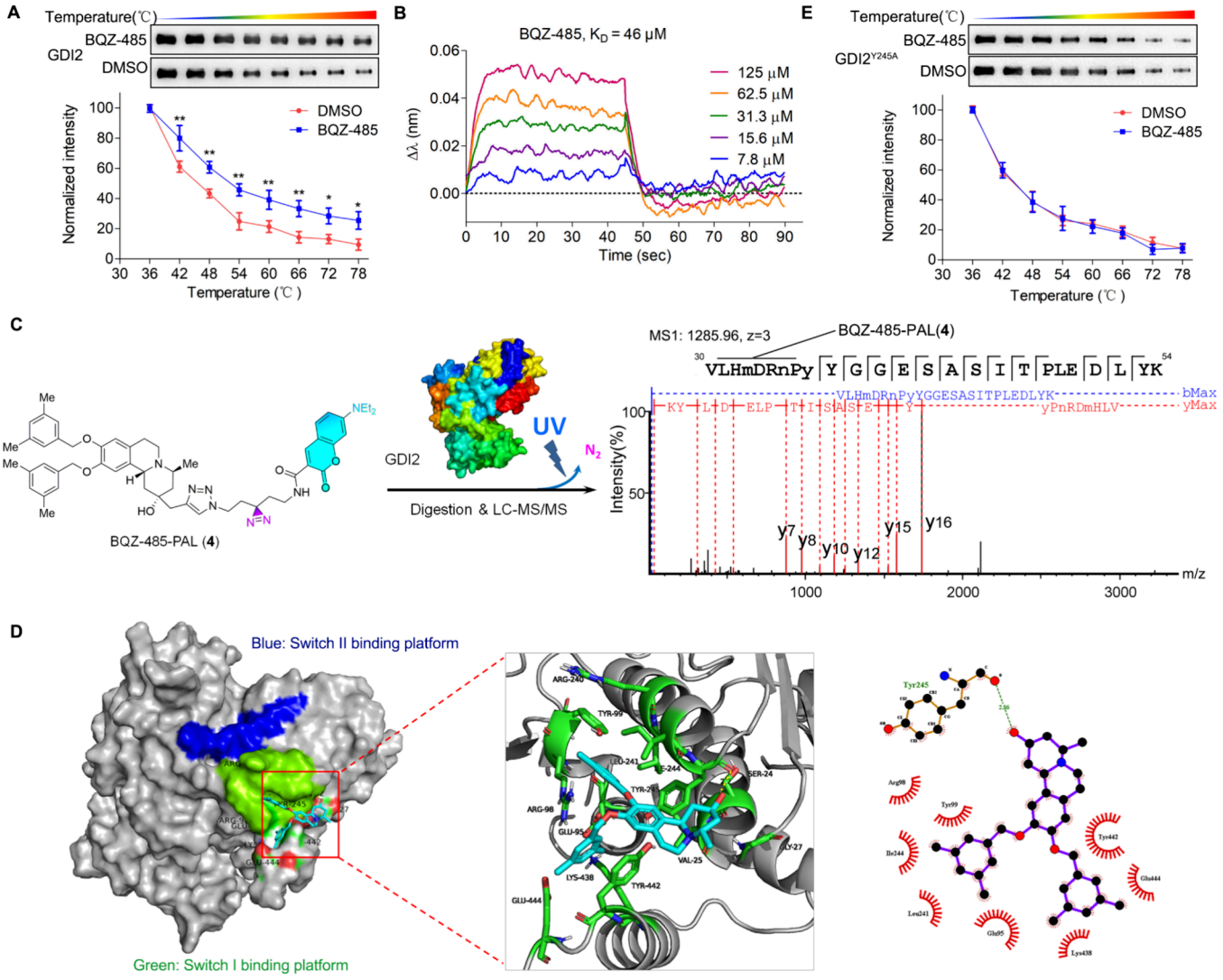

Figure 2. BQZ-485 binds to the RBP domain of GDI2. (A) Thermal stability of GDI2 with BQZ-485 (10 μM, 4 h, 4 °C, n = 3) by CETSA, $^{**}p <$ 0.01 vs control. (B) Binding affinity of BQZ-485 to GDI2 determined by BLI titrations (7.8−125 μM), with a K_D of 46 μM. (C) BQZ-485 derived photoaffinity probe (**4**) and LC-MS/MS analysis of the BQZ-485-PAL bound peptide sequence. Photo-cross-linking was initiated by UV irradiation. The resulting adduct was then subjected to protein digestion and submitted to LC-MS/MS analysis. The MS/MS spectrum shows the BQZ-485-PAL labeled a ^{30}VLHMDRNPYYGGESASITPLEDLYK^{54} peptide. (D) Predictive binding mode of BQZ-485 in the GDI2 protein. The interaction interface is composed of Glu95, Arg98, Tyr99, Leu241, Ile244, Tyr245, Tyr442, Lys438, Tyr442, and Glu444. The H-bond with Y245 is highlighted. The GDI2 protein was subjected to homology modeling using AlphaFold 2.0 (AF-P50395-F1-model_v1), and docking simulation was implemented by SYBYL-X 2.1.1 and analyzed by LigPlot$^+$. (E) Thermal stability of recombinant GDI2^{Y245A} (1 μM) with or without BQZ-485 (10 μM, 4 h, 4 °C) by the CETSA (n = 3).

significant synergistic antiproliferative effect (Figure 1J). By overexpressing the GDI2 protein, we performed an additional rescue experiment that notably diminished the lethality of BQZ-485 (Figure S2F,G), providing further validation to GDI2 as the primary target for BQZ-485. These preliminary findings demonstrated that GDI2 serves as the molecular target of BQZ-485 for activating the downstream paraptosis machinery.

BQZ-485 Bound to the RBP Domain of GDI2

To verify the interaction between BQZ-485 and GDI2, we conducted a cellular thermal shift assay (CETSA), which indicated that the target engagement of BQZ-485 with GDI2 is in the low micromolar range (Figure 2A). Furthermore, the binding affinity was quantified by a biolayer interferometry (BLI) assay[44] and the dissociation constant (K_D) value of BQZ-485 was determined to be 46 μM (Figure 2B). Although this binding affinity value represents a moderate intracellular binding affinity between BQZ-485 and GDI2, it is comparable to the binding affinity observed between GDI and its native binding partner, Rabs.[45,46] The discrepancy between the K_D value and the cellular IC_{50} of BQZ-485 can be attributed to the inherent differences between the intracellular and extracellular experiments, for example, the differences in the concentration of GDI2 and different biological responses used in the tests.

Intrigued by the binding results, we attempted to identify the BQZ-485 binding pocket and locate the key residues. Despite numerous attempts, we were unable to obtain crystals of the GDI2/BQZ-485 complex suitable for diffraction. Instead, we decided to employ photoaffinity labeling (PAL) combined with LC-MS/MS-based proteomic analysis as an alternate strategy for identifying the binding site with atomic-level precision.[47] In the presence of diazirine-containing

https://doi.org/10.1021/jacsau.3c00228
JACS Au 2023, 3, 2749−2762

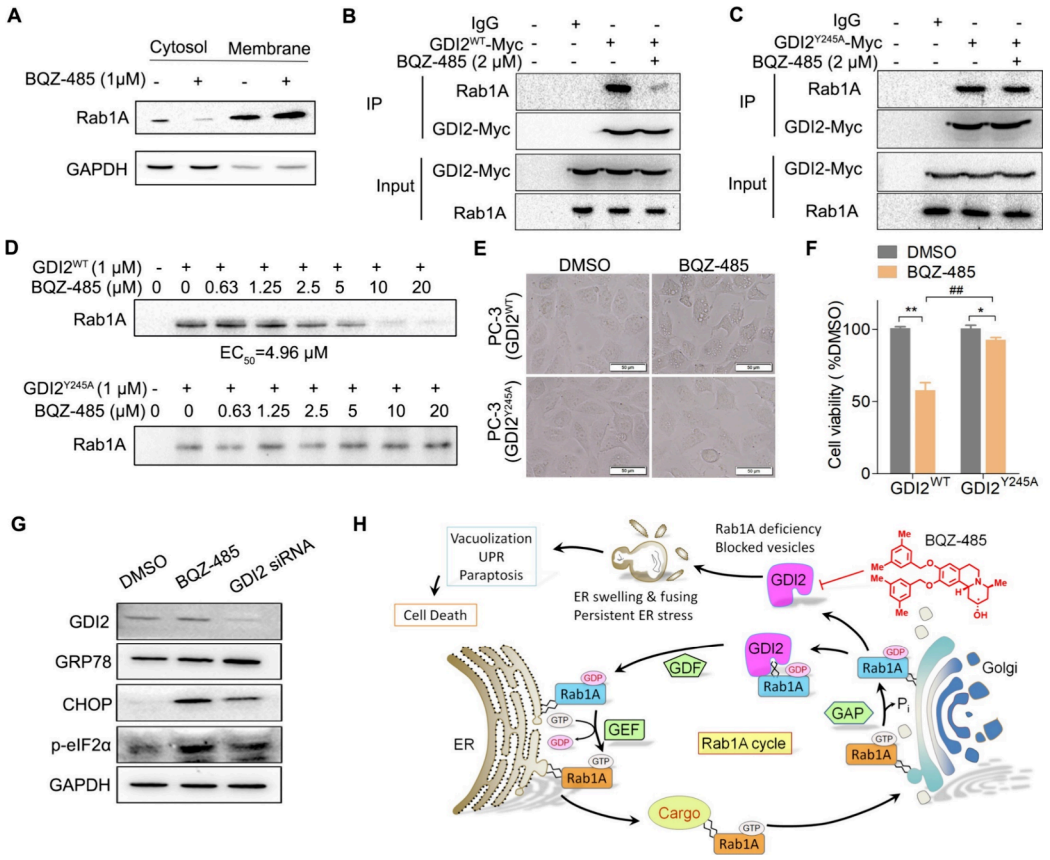

Figure 3. Mechanistic investigation of BQZ-485 induced paraptotic cell death. (A) Western blot level of Rab1A in the cytoplasm and membrane of PC-3 cells after BQZ-485 treatment (2 μM, 24 h). (B, C) Co-immunoprecipitation of Rab1A and GDI2 (B, GDI2^{WT}-Myc; C, GDI2^{Y245A}-Myc). PC-3 cells were treated with BQZ-485 (2 μM, 24 h) and immunoblotted with anti-GDI2 or anti-Rab1A antibody. (D) Western blot level of membrane Rab1A retrieved by GDI2. Membrane extracts from PC-3 cells were preloaded with GDP (1 mM, 45 min, 37 °C) and incubated with GDI2^{WT} (1 μM) or GDI2^{Y245A} (1 μM) for 30 min. Mixtures were centrifuged and pelleted, and then the resulting soluble fractions were analyzed by Western blot. (E) Representative vacuolization images in PC-3-GDI2^{WT}-Myc and PC-3-GDI2^{Y245A}-Myc cells after BQZ-485 treatment (2 μM, 48 h). Scale bars: 10 μm. (F) Cell viability in PC-3-GDI2^{WT}-Myc and PC-3-GDI2^{Y245A}-Myc cells after BQZ-485 treatment (2 μM, 48 h). Scale bars: 10 μm. Significance: *$p < 0.05$, **$p < 0.01$; $^{\#\#}p < 0.01$. (G) Western blot analysis of ER stress/UPR markers GRP78, CHOP, and p-eIF2α in PC-3 cells that were treated with DMSO, BQZ-485 (1 μM, 24 h), or GDI2 siRNA. GAPDH as loading controls. (H) Summary of Rab1A-GDI2-involved antegrade ER−Golgi vesicle trafficking and the effect of BQZ-485.

fluorescence probe BQZ-485-PAL (**4**; Figure S3A), we found that the peptide sequence ^{30}VLHMDRNPYYGGESASIT-PLEDLYK^{54} was covalently modified by the UV-generated triplet carbene (892.4887 Da, calcd for $C_{54}H_{64}N_6O_6^{2\bullet}$). Further tandem mass analysis identified ^{30}VLHMDRNPY^{38} as the labeled site (Figure 2C). Thus, domain I of GDI2 was determined to be the binding site of BQZ-485. Due to the absence of a reported GDI2 structure, homology modeling of GDI2 was conducted with AlphaFold2[48] and ligand docking simulations were performed. After focusing on ribbon cavities located in the vicinity of the Val30−Tyr38 residues, molecular docking simulation indicated that BQZ-485 effectively occupied a partial surface of the RBP ribbon (Rab binding platform) of GDI2. A hydrogen bond with Tyr245 and hydrophobic interactions with other residues were found (Figure 2D), indicating that BQZ-485 has the potential to competitively displace the native substrate, Rabs, and prevent the C-terminus coordinating region (CCR) cavity on GDI2 from recognizing the Rab C-terminal characteristic sequence (AXA box), thereby resulting in the arrest of the assembly of the Rab-GDI2 cocomplex.

To experimentally validate the engagement of BQZ-485 with the RBP pocket, we prepared a recombinant Y245A mutant protein, GDI2^{Y245A} (Figure S3B), to alter the geometry of the binding pocket and diminish BQZ-485 binding. In contrast to GDI2^{WT}, *in vitro* thermal shift results demonstrated that the mutation Y245A abolished the interaction between BQZ-485 and GDI2^{Y245A} (Figure 2E), which is in agreement with our theoretical prediction. These results clearly showed that GDI2 is a *bona fide* molecular target of BQZ-485 and that the Tyr245-involved Rab binding platform (RBP) domain is the key pocket for BQZ-485 binding.

BQZ-485 Disrupted GDI2-Rab1A Interaction, Abrogated ER-to-Golgi Vesicle Transport, and Induced ER-Associated Paraptosis

Having elucidated the molecular basis of the interaction between BQZ-485 and GDI2, we next investigated how GDI2 inhibition facilitates ER dilation, induces vacuolization, and reprograms cell fate. GDI2 is well-known for its function of recycling Rabs from their target membrane back to the vesicular pool. Likewise, Rab1A, which is known to be an important substrate of GDI2, is located on the ER membrane and controls vesicle targeting for protein transport from the ER to the Golgi apparatus.[49] We therefore investigated the response of Rab1A to GDI2 inhibition. We observed that

https://doi.org/10.1021/jacsau.3c00228
JACS Au 2023, 3, 2749−2762

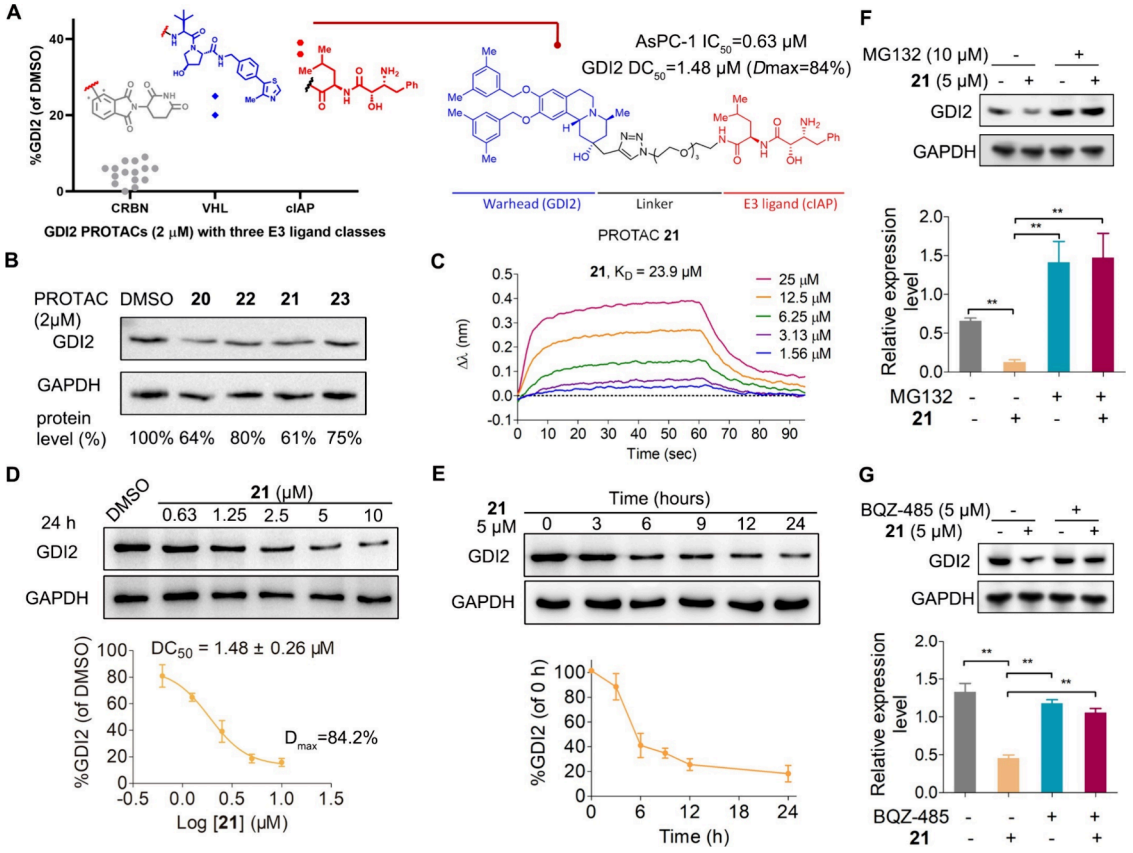

Figure 4. Discovery of the GDI2 degrader. (A) Scattergraph representation of GDI2 degradation efficacies by the PROTACs with three types of E3 ligands and the chemical structure of **21**. (B) Western blot analysis of GDI2 levels in the presence of compounds **20**−**23** (2 μM, 24 h). PC-3 cells were treated with compounds **20**−**23**, and the lysates were submitted for Western blot analysis. (C) Binding affinity of **21** for GDI2 by the BLI assay (1.56−25 μM), K_D = 23.9 μM. (D) Compound **21**-induced dose-dependent degradation of GDI2 and representative Western blot image in AsPC-1 cells (0.63−10 μM, 24 h, n = 3). GAPDH as the loading control, DC_{50} = 1.48 μM, D_{max} = 84.2%. (E) Time course of **21**-mediated GDI2 degradation by Western blot analysis (0−24 h, n = 3). (F, G) Western blot analysis of GDI2 degradation induced by **21** with pretreatment of MG132 or BQZ-485. AsPc-1 cells were pretreated with either MG132 (5 μM) or BQZ-485 (5 μM) for 4 h and treated with compound **21** for 24 h.

BQZ-485 induced abnormal distribution of Rab1A: specifically, there was substantial depletion in the cytosol but accumulation in the membrane (Figure 3A), indicating that the intrinsic GDI2-Rab1A interaction was disrupted and that intracellular Rab1A recycling was severely impaired. To further confirm that treatment with BQZ-485 abrogated the GDI2-Rab1A interaction in live cells, $GDI2^{WT}$-Myc and $GDI2^{Y245A}$-Myc proteins were transfected into PC-3 cells. The co-immunoprecipitation results showed that the intracellular $GDI2^{WT}$-Rab1A interaction was significantly disrupted by BQZ-485, but the interaction of $GDI2^{Y245A}$ with Rab1A was not affected (Figure 3B,C). *In vitro* Rab1A retrieval assays revealed that BQZ-485 profoundly suppressed the activity of $GDI2^{WT}$ in Rab1A extraction, with an EC_{50} value as low as 4.96 μM, but was completely ineffective against the mutant $GDI2^{Y245A}$ protein (Figure 3D and Figure S4A). Additionally, in comparison to $GDI2^{WT}$ cells, $GDI2^{Y245A}$ mutant cells showed significant resistance to BQZ-485 induced cell death and cellular vacuolization (Figure 3E,F).

Disruption of Rab1A homeostasis resulting from GDI2 inhibition is expected to lead to the blockade of anterograde ER-to-Golgi protein trafficking and exacerbate the accumulation of unfolded proteins in the ER lumen. We observed that attenuating *de novo* protein synthesis (and thus the aggregation of unfolded proteins) by treatment with cycloheximide (CHX), actinomycin-D (Act-D), or 4-phenylbutyric acid (4-BPA) could effectively reverse both the vacuolization and cell death caused by BQZ-485. Once the ER becomes overloaded with unfolded proteins after BQZ-485 treatment, hypertonic administration of mannitol is able to counter the increasing ER osmolarity, resulting in the alleviation of ER cisternae dilation and cell mortality (Figure S4B,C). Regarding the signaling pathway, inactivation of GDI2 by either BQZ-485 or GDI2 siRNA was shown to trigger the UPR during ER stress, as upregulation of glucose-regulated protein GRP78 and phosphorylation of eukaryotic initiation factor (p-eIF2α) and CHOP were observed in cells by Western blot analysis when inhibiting or silencing of GDI2 (Figure 3G and Figure S4G). It is well-known that the terminal UPR failed to restore ER proteostasis in most cases.[50] The unfold proteins are prone to aggregation, leading to persistent proteotoxicity and, eventually, cell death.

Given the essential role of post-translational prenylation of Rabs for their membrane affinity,[51] downregulating prenylated Rab1A is an alternative approach to trigger parpatosis and exhibit synergy with the GDI2 inhibitor BQZ-485. It is well-known that the synthesis of mevalonate metabolite geranylgeranyl pyrophosphate (GGPP) and subsequent geranylgeranyl transfer are essential for the prenylation of Rabs[52] (Figure S4D). We therefore blocked this signaling pathway using the HMG-CoA reductase inhibitor atorvastatin, GGPP synthase inhibitor NE10790, and Rab geranylgeranyl transferase

https://doi.org/10.1021/jacsau.3c00228
JACS Au 2023, 3, 2749−2762

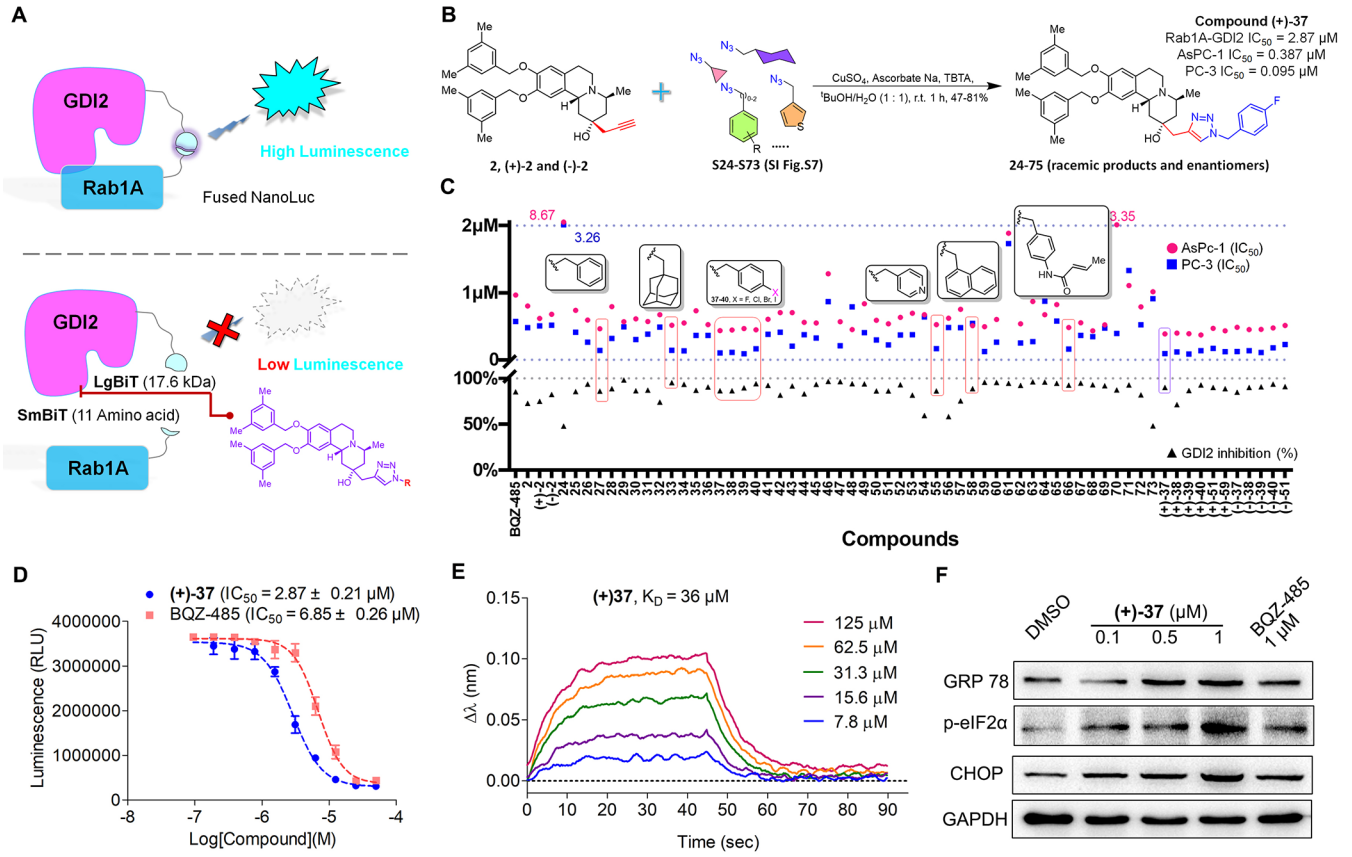

Figure 5. Click chemistry and the NanoLuc-based platform leading to more potent GDI2 inhibitors. (A) Schematic representation of the NanoLuc-based system for quantifying the GDI2-Rab1A interaction. Once LgBiT-tagged GDI2 interacts with SmBiT-tagged Rab1A, the complementary fragments of nanoluciferase fused to reconstitute luminescence activity. The chemical inhibitors (red) are supposed to disrupt the interaction and attenuate the luminescence. (B) Click chemistry leading to novel GDI2 inhibitors. The most optimized analogue is (+)-**37.** (C) Scattergraph representation of the inhibitory potencies of novel benzo[*a*]quinolizidine derivatives at the protein and phenotypic levels. GDI2 inhibition rate (%) at 6.25 μM and the IC_{50} values for PC-3 and AsPC-1 cells were displayed. (D) Dose−response curves of GDI2-Rab1A interaction inhibition in the presence of (+)-**37** and BQZ-485 (0.1−50 μM), IC_{50} = 2.87 and 6.85 μM. (E) BLI binding studies of (+)-**37** to GDI2 (7.8−125 μM), K_D = 36 μM. (F) Western blot analysis of ER stress and UPR markers in (+)-**37** or BQZ-485 treated AsPC-1 cells (24 h).

inhibitor YM-529 to decrease the synthesis of prenylated Rab1A and investigated their effect on the induction of paraptosis. As expected, these inhibitors were able to induce slight paraptosis when used individually and synergistically enhanced the antiproliferative potency of BQZ-485 (Figure S4E,F).

As summarized in Figure 3H, our data clearly indicate that inhibiting GDI2 by BQZ-485 impaired ER-associated vesicular transport and led to ER swelling/dysfunction, which in turn resulted in an extensive cytoplasmic vacuolization phenotype and steered cell fate toward death. This mechanism illustrates that targeting GDI2 for paraptosis holds great potential for improving cancer therapy.

Chemical Knockdown of GDI2 Induces Paraptosis to Enhance Cancer Therapy

Targeting protein degradation is a revolutionary technology for achieving chemical knockdown of a targeted protein and is widely used in drug discovery. Dozens of bifunctional PROTACs have been developed to hijack the intrinsic cellular ubiquitin−proteasome system to degrade specific proteins and thereby provided clinical benefit.[53] Thus, by leveraging the direct binding affinity of BQZ-485 to GDI2, we attempted to develop novel GDI2 degraders via a versatile design strategy. The chemical expansion was principally focused on the investigation of linkers/E3 ligands (Figure 4A; all structures are shown in Figure S5). In this preliminary exploration, the optimized degrader **21** stood out with high potencies for both GDI2 degradation and antiproliferative activity against PC-3 cells and GDI2-overexpressing pancreatic cancer cell line AsPc-1 cells (Figure 4A,B, Figure S6A, and Table S5). The sufficient binding affinity of **21** to GDI2 (Figure 4C; K_D = 23.9 μM) is fundamental to its intracellular degradation ability. The Western blot analysis clearly shows that **21** efficiently degraded the target protein in both time- and concentration-dependent manners in AsPC-1 cells, as >70% of GDI2 was depleted after 9 h of treatment, and a DC_{50} value of 1.48 μM was determined (Figure 4D,E; D_{max} = 84.2% at 10 μM).

Moreover, we conducted an additional mechanism investigation to demonstrate that degrader **21** induces GDI2 degradation through the ubiquitin−proteasome system. In the presence of the proteasome inhibitor MG132, **21**-induced GDI2 degradation was significantly prevented (Figure 4F), highlighting its reliance on proteasome. We observed that pretreatment with the competitor BQZ-485 prevented the degradation of GDI2 by **21**, providing further evidence that binding of **21** by GDI2 was essential for promoting degradation (Figure 4G). Meanwhile, the transcription level

https://doi.org/10.1021/jacsau.3c00228
JACS Au 2023, 3, 2749−2762

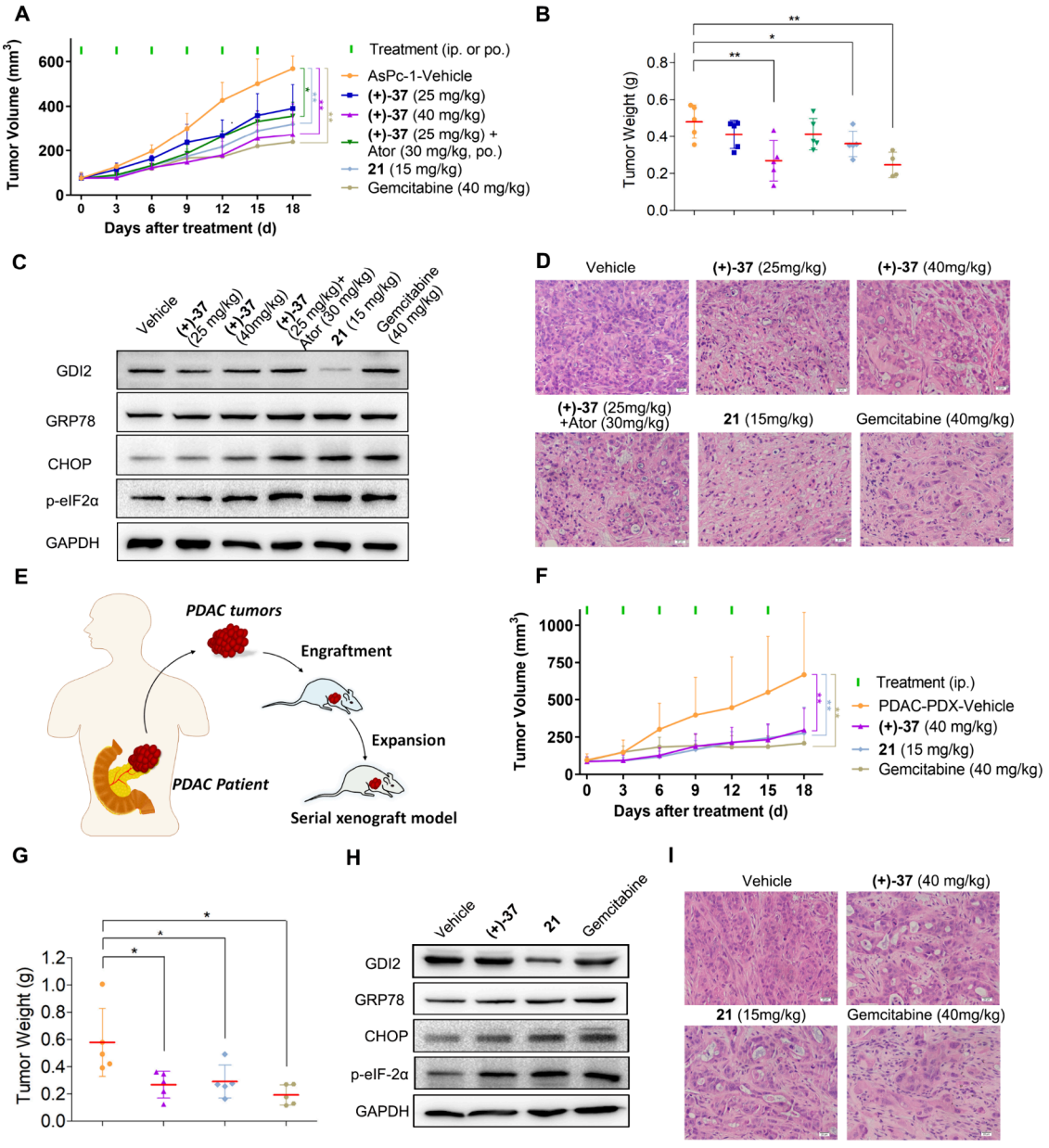

Figure 6. Compound **21** and (+)-37 suppress tumor growth in the AsPC-1 xenograft model and the pancreatic adenocarcinoma PDX model. (A) Growth curve of tumor volume, $*p < 0.05$, $**p < 0.01$, compared to the vehicle group ($n = 5$). (B) Weight of dissected tumors after treatment. (C) Western blot analysis of GDI2, GRP78, CHOP, and p-eIF2α proteins in tumor tissues. (D) Representative H&E staining of the tumor sections. Scale bars: 20 μm. (E) Schematic outline of the establishment of the pancreatic adenocarcinoma PDX model. (F) Growth curves of pancreatic adenocarcinoma PDX tumors in nude mice during treatment ($n = 5$). $**p < 0.01$, compared to the vehicle group. (G) Dissected tumor weight collected after treatment. $*p < 0.05$ vs vehicle. (H) Protein levels of GDI2, GRP78, CHOP, and p-eIF2α in tumor tissue analyzed by Western blot. (I) Representative images of tumor sections that underwent H&E staining. Scale bars: 20 μm.

of GDI2 was not affected by **21**, as the qPCR analysis of GDI2 mRNA, which showed no discernible difference (Figure S6B), and the autophagy inhibitor chloroquine (CQ) did not exert any impact on the restoration of the GDI2 protein level (Figure S6C). In addition, degrader **21** selectively induces GDI2 degradation without affecting the GDI1 protein level up to 10 μM (Figure S6D,E). This discovery opens up novel therapeutic possibilities for exploiting GDI2 degraders for cancer treatment.

Click Chemistry and High-Throughput Platform Enable Us to Discover More Potent BQZ-485 Derivatives for Targeting the GDI2-Rab1A Interaction

To enable the high-throughput screening of GDI2 inhibitors for the induction of paraptosis, we developed a facile NanoLuc-based protein-fragment complementation assay (NanoPCAs) to quantify the GDI2-Rab1A interaction *in vitro*. The native binding process of GDI2 with inactive GDP-Rab is composed of two consecutive steps: (1) Rab recognition (low-affinity complex) and (2) transfer of Rab geranylgeranyl groups (high-affinity complex).[54] Potential inhibitors are proposed to directly target GDI2 RBP in the first step, disrupting its hydrophobic contacts with Rab1A. In addition,

https://doi.org/10.1021/jacsau.3c00228
JACS Au 2023, 3, 2749−2762

unprenylated Rabs have beenreported to interact with GDI,[45,46] and we thereby use the unprenylated Rab1A as the GDI2 interaction partner in our NanoLuc system to avoid performing post-translational modifications. GDI2-LgBiT and SmBiT-Rab1A were expressed in *Escherichia coli*, respectively (Figure S7A), and then the *in vitro* GDI2-Rab1A interaction could be visualized by luminescence when the split NanoLuc fragments were brought into close proximity (Figure 5A). In the presence of chemical inhibitors, the inhibitory rate of the GDI2-Rab1A interaction could be quantified by the decrease in luminescence.

Based on the predicted binding mode of BQZ-485 in GDI2, we pursued further modifications of BQZ-485 focused on the construction of various C_2 triazole branches to occupy enlarged target surfaces and provide extra hydrophobic interactions (Figure S7B). Starting from BQZ-485 alkyne intermediate **2**, CuAAC click chemistry enabled us to construct a small library of novel benzo[*a*]quinolizidines for screening (Figure S7B; individual structures are shown in Figure S7B). Most analogues inhibited the interaction of GDI2 with Rab1A by over 70% at 6.25 μM (Figure 5C and Table S6), and their potencies in the *in vitro* assay were positively correlated with antiproliferative activities in GDI2-overexpressed AsPC-1 and PC-3 cells (Figure 5C and Table S6). To evaluate the toxicity of selected compounds, we also determined their potency against a GES-1 human gastric epithelium cell line, revealing that most compounds exhibited at least a 10-fold greater activity in the cancer cells (Figure S7C). Comprehensive consideration of the potency and selectivity suggested that the enantiomer (+)-**37** (Figure 5C), with a 4-fluorobenzyl triazole branch, was the optimum GDI2 inhibitor for both impairing the GDI2-Rab1A interaction and inducing cell death via paraptosis (Figure S7D,E). The K_D value of (+)-**37** for GDI2 was 36 μM, which slightly increased compared to that of BQZ-485, and the potency in inhibiting the GDI2-Rab1A interaction increased by 2.5-fold ((+)-**37**, 2.87 μM vs BQZ-485, 6.85 μM; Figure 5D,E). At the cellular level, the persistent ER stress, lethal UPR signaling, and vacuolization phenotype attributed to ER dysfunction were confirmed in AsPC-1 cells in the presence of a low concentration of (+)-**37** (Figure 5F). Thus, (+)-**37** is an improved GDI2 inhibitor and warrants further *in vivo* investigation.

Compound 21 and (+)-37 Suppress Pancreatic Cancer Progression and Induce Tumor Cell Paraptosis in a Mouse Xenograft Model

To investigate the *in vivo* antitumor efficacy of GDI2 targeting degrader **21** and inhibitor (+)-**37**, we first developed an AsPC-1 pancreatic carcinoma xenograft model with a high expression of GDI2. When tumors in the dorsal region were palpable (~100 mm^3), mice were randomized into six groups and treated with vehicle, (+)-**37** (25 mg/kg, ip.; 40 mg/kg, ip.); **21** (15 mg/kg, ip.), or gemcitabine (40 mg/kg, ip.). A group treated with (+)-**37** in combination with atorvastatin (25/30 mg/kg, ip./po.) was also included to investigate *in vivo* synergistic effects between GDI2 inhibition and prenylated Rab insufficiency. After 18 days of treatment (6 doses; Figure 6A), both (+)-**37** and **21** significantly attenuated tumor growth compared to the vehicle group, presumably by suppressing or degrading GDI2 (Figure 6A,B; the dissected tumors are shown in Figure S8A). Disappointingly, there was no *in vivo* synergism when (+)-**37** was combined with atorvastatin, which we ascribe to an insufficient concentration of atorvastatin *in vivo*. No significant signs of toxicity were observed in the mice of the (+)-**37** and **21** treatment groups, as no body weight loss in the treatment group, while histopathological examination of dissected major organs (heart, lung, liver, spleen, and kidney) showed no signs of injury compared to the vehicle group (Figure S8B,C). Histopathological examination of the dissected tumors revealed extensive cytoplasmic vacuolization in the degrader and inhibitor treatment groups, implying that these tumors underwent paraptosis and their invasiveness was attenuated (Figure 6)D. According to Western blot analysis, long-lasting GDI2 depletion by **21** was achieved *in vivo*, as more than 90% of GDI2 was not restored even at 72 h post final injection (Figure 6C and Figure S8D). The protein levels of GRP78, CHOP, and p-eIF2α in tumor tissue were elevated due to the occurrence of ER stress and UPR activation in tumor tissues, which is in accordance with the *in vitro* data (Figure 6D and Figure S8D). In addition, we demonstrated that the treatment groups did not exhibit a significant decrease in Rab1 expression (Figure S8E).

Pancreatic carcinoma patient-derived xenograft (PDX) models allow for the faithful reproduction of human pancreatic cancer biology and offer an opportunity to evaluate the therapeutic response to potential chemotherapies in a more realistic context. To this end, a PDX tumor model of pancreatic adenocarcinoma (PDAC) was established (Figure 6E). Resected PDAC tumors and adjacent benign tissues were collected from the Qilu Hospital, Jinan, China. IHC staining revealed that GDI2 expression in cancerous tissues was significantly higher than that in adjacent normal tissues (Figure S9A). As described in the procedure, we transplanted PDX fragments into nude mice, and the third-generation PDX mice were successfully established for *in vivo* study. Two weeks post implantation, mice were assigned to receive treatment with vehicle, (+)-**37** (40 mg/kg, ip.), **21** (15 mg/kg, ip.), or gemcitabine (40 mg/kg, ip.) for 18 days. Consistent with the previous results in the conventional AsPC-1 xenograft model, both GDI2 inhibitor (+)-**37** and degrader **21** successfully suppressed PDAC tumor growth (Figure 6F,G; the the dissected tumors are shown in Figure S9B) to levels similar to those of the gemcitabine treatment group without significant toxicity (Figure S9C,D). The cytoplasmic vacuolization and increased GRP78, CHOP, and p-eIF2α levels confirmed the disruption of ER homeostasis, as well as subsequent terminal UPR activation, in the PDAC−PDXs (Figure 6H,I and Figure S9E). Notably, degrader **21** still exhibited excellent potency in eliminating GDI2 in PDAC tumors (Figure 6H and Figure S9E). These findings provided evidence that inducing paraptosis by targeting GDI2 is a promising therapeutic strategy for pancreatic cancer therapy, and both GDI2 inhibitors and degraders could bring clinical benefits to patients with pancreatic cancers.

CONCLUSIONS

Overexpression of GDI2 has been recognized as a diagnostic and prognostic biomarker in various tumor tissues,[8,55−58] especially in pancreatic and hepatocellular carcinomas, but its potential as a target for new cancer therapy had not been investigated previously. In this study, we used ABPP to identify that GDI2 plays a critical role in paraptosis and demonstrated that BQZ-485 can serve as a potent inhibitor of GDI2. BQZ-485 binds to GDI2, which impairs Rab1A retrieval, abolishes ER-to-Golgi vesicle transport, and reprograms cell fate to paraptotic cell death. We created a small library of BQZ-485

https://doi.org/10.1021/jacsau.3c00228
JACS Au 2023, 3, 2749−2762

analogues, from which we discovered a more potent GDI2 inhibitor ((+)-37). In addition, we leveraged BQZ-485's engagement with GDI2 to develop the selective PROTAC molecule **21** as a GDI2 degrader. The optimized inhibitor (+)-37 and degrader **21** described in this study exhibited excellent *in vivo* antitumor activity in two pancreatic cancer xenograft models, including an AsPc-1 solid tumor model and a transplanted human PDAC tumor model. Our findings provide clear evidence that the induction of paraptosis by targeting GDI2 with benzo[*a*]quinolizidine analogues is a promising strategy for enhancing cancer therapy.

METHODS

SILAC-ABPP Assay

PC-3 cells were passaged 10 times in SILAC DMEM (Thermo Fisher Scientific) with 10% dialyzed fetal bovine serum (dFBS) (Thermo Fisher Scientific), 1% penicillin−streptomycin, and 100 μg/mL [$^{13}C_6$,$^{15}N_4$] L-arginine-HCl and [$^{13}C_6$,$^{15}N_2$] L-lysine-HCl or L-arginine-HCl and L-lysine-HCl (Thermo Fisher Scientific). The cells were harvested and stored at −80 °C for further experiments. Frozen cell pellets were resuspended in IP lysis buffer (Beyotime), sonicated, and separated into soluble and insoluble fractions by centrifugation at 15,000*g* for 20 min. The soluble protein concentration was determined using the BCA protein assay (Beyotime). The lysates were adjusted to 2 mg/mL and treated with 10 μM compound **3** or DMSO at 4 °C with agitation overnight. The DMSO-treated light proteome and heavy probe-labeled proteome were mixed equally in a 1:1 ratio and preincubated with streptavidin agarose (Thermo Fisher Scientific) for 30 min at room temperature. The beads were washed six times with PBS and the bead-bound proteins in SDS loading buffer were boiled for 10 min. The beads were centrifuged, and the supernatant was collected, with the eluted proteins separated by SDS-PAGE and the protein-containing bands in the gel excised, followed by in-gel digestion. The samples were analyzed by LC-MS/MS analysis (Applied Protein Technology, Shanghai, China).

RNA Interference and GDI2 Overexpression

The siRNA constructs as listed below (Table S2) were designed and synthesized by Sangon Biotech (Shanghai, China). The interference was performed based on the protocol of HighGene Transfection reagents (ABclonal, Wuhan, China). Human GDI2 genes were inserted in the pcDNA3.1 (+) vector, and the empty vector was used as the negative control. Cells were plated in 6-well plates and cultured overnight. Then cells were transfected with 2 μg of vector DNA using HighGene Transfection reagents (ABclonal, Wuhan, China). After treatment, the cells were harvested and processed for further analysis.

Co-Immunoprecipitation Assays

The GDI2^{WT} and GDI2^{Y245A} overexpressing cells were treated with BQZ-485 (2 μM) or DMSO for 12 h, respectively. After treatment, the cells were harvested and lysed with IP lysis buffer (Beyotime) containing a protease inhibitor. The samples were subsequently prepared according to the instructions of the Immunoprecipitation Kit (Proteintech, Wuhan, China). Supernatants were collected and incubated with anti-Myc antibody or mouse IgG overnight at 4 °C. Protein agarose beads were mixed at room temperature for 2 h and then centrifuged to obtain the precipitate. After purification using elution buffer, the antigen−antibody mixtures were treated with basic neutralization buffer and analyzed by Western blot.

Rab1A Retrieval Assay

PC-3 cells (serum-starved for 5 h before the experiment) were washed twice prior to homogenization at 4 °C in the "homogenization buffer" (50 mM Hepes/KOH, pH 7.6, 1 mM EDTA, 5 mM $MgCl_2$, 1 mM GDP, and 1× phosphatase inhibitor mixture). Plasma membrane fraction was obtained after two consecutive centrifugations: 10 min at 800*g* and 20 min at 15,000*g* at 4 °C. Equal amounts (typically 100 μg of membrane proteins) were pretreated for 45 min at 37 °C with GDP (1 mM) and incubated in the presence of either GDI2^{WT} (1 μM) or GDI2^{Y245A} (1 μM) with different concentrations of BQZ-485 in a reaction buffer (50 mM Hepes/KOH, pH 7.6, 5 mM $MgCl_2$, 1 mM DTT, and supplemented with 1× phosphatase inhibitor mixture). The reaction mixtures were pelleted (10 min, 15,000*g*), and the soluble fractions were analyzed for Rab1A contents by Western blot.

BLI Assays

BLI assays were performed by a standard procedure according to the manufacturer's introduction. In brief, the BLI experiments were performed by an Octet RED96E instrument (ForteBio, Port Washington, NY, USA). The recombinant GDI2^{WT} protein was first captured by electrostatic interactions onto APS biosensors. Then, the baseline signal was established by incubating with buffer (300 s equilibration). The candidate compounds were dissolved with pH 7.4 SD + 5% DMSO buffer (125−7.8 μM or 25−1.56 μM, 2-fold dilution), and the resulting solution was added to a 96-well plate for wetting the GDI2-bound APS biosensors. The equilibration was allowed to proceed for a total duration of 50 s until a saturation response was reached. Tips were washed in dissociation buffer for 90 s to block unbound hydrophobic sites and establish second base lines. Consecutive association−dissociation cycle programs were performed in the presence of the tested compounds. Acquired raw data were processed in the analysis software provided by the manufacturer using double reference subtraction. The resulting data were fitting with a 1:1 binding model to afford the k_{on} and k_{off} values, and then K_D values were obtained.

PAL Experiment

Purified GDI2^{WT} was adjusted to 10 μM and treated with 10 μM BQZ-485-PAL for 60 min. After probe labeling, the protein was irradiated under UV light (365 nm) for 5 min on ice to covalently cross-link the probe with the target site. And then the protein was separated by SDS-PAGE and the protein-containing band in the gel was excised, followed by in-gel digestion. The samples were analyzed by LC-MS/MS analysis (Applied Protein Technology, Shanghai, China).

Molecular Docking Analysis

The homology model of human GDI2 (AF-P50395-F1-model_v1) was obtained from AlphaFold2. Potential binding pockets inside the protein were predicted using the information obtained from the PAL experiment as constraints. We predocked BQZ-485 into a binding pocket in domain I of GDI2 using SYBYL-X. The results were analyzed by PyMOL and LigPlot$^+$.

NanoLuc PCA

The sequences (Supporting Information) of GDI2-LgBiT and SmBiT-Rab1A were synthesized and cloned into SUMO-pET28a by Sangon Biotech (Shanghai, China). The plasmids were transformed into *E. coli* BL21 and cells were grown in LB media, and the expression of proteins was induced by 0.1 mM IPTG at 18 °C. The protein purification used the same procedure in Supporting Information.

For inhibitor testing, chemical compounds were dissolved to 100 μM and 2-fold serially diluted in PBS. GDI2-LgBiT (40 μL) (1.25 μM in PBS) was added to 96-well plates and then mixed with 20 μL of compound at the desired concentrations. The mixture was incubated for 60 min at 37 °C. The 40 μL portion of SmBiT-Rab1A (5 μM in PBS) was then added to each well, followed by incubation for 30 min at 37 °C. After the final incubation step, an equal volume of Promega Nano-Glo Luciferase Assay Substrate was added to the reaction mixture. Emitted luminescence was measured by using a microplate reader (Bio-Tek).

Immunofluorescence Assay

PC-3 cells were plated on coverslips in 6-well plates. After 24 h, the culture medium was removed and replaced with medium containing BQZ-485 or vehicle control. At the indicated time points, the cells were fixed for 10 min with 4% formaldehyde. The coverslips were washed with PBS and permeabilized for 5 min with 0.5% Triton X-100 in PBS. Following PBS washing, the coverslips were blocked for

https://doi.org/10.1021/jacsau.3c00228
JACS Au 2023, 3, 2749−2762

30 min at room temperature with 1% BSA in PBS. The coverslips were then incubated overnight at 4 °C with primary antibodies. The coverslips were washed with PBS and incubated for 60 min at room temperature with TRITC-conjugated secondary antibodies, including incubation with DAPI for the final 10 min. The coverslips were then washed sequentially with PBS and mounted on microscope slides. Imaging data was acquired using a Zeiss LSM 780 scanning confocal microscope.

Tumor Xenograft Model and Treatment

Male BALB/c athymic nude mice (6−8 weeks) were purchased from the SPF (Beijing) Biotechnology (Beijing, China) and maintained at the Animal Experimental Center in the School of Pharmaceutical Sciences (Shandong University).

Gemcitabine is the clinical standard drug for treating pancreatic cancer. Based on the assessment of our coauthor who is a specialist physician in pancreatic cancer and results from pretests, a dosage of 40 mg/kg gemcitabine is an appropriate positive control for research purposes.[59−61] To investigate the *in vivo* antitumor effect of (+)-**37** in pancreatic cancer and compare it with that of gemcitabine, a dosage of 40 mg/kg (+)-**37** was determined for *in vivo* experiments. Furthermore, a lower dosage of 25 mg/kg was used for dose−response and drug-combination evaluation. Due to the limited solubility, a dosage of 15 mg/kg for compound **21** was established, which is equivalent to approximately 0.375 mg in a volume of 0.2 mL solvent for a 25 g mouse.

For the pancreatic cancer (AsPC-1) xenograft model, AsPC-1 tumor cells (5×10^6) were suspended in sterile PBS (100 μL) and inoculated subcutaneously in the right flank of nude mice. Two weeks after the injection of cells, when the tumors became palpable (around 100 mm^3), mice were randomly divided into six groups (n = 5 per group) and received equal amounts of solvent (ip.), (+)-**37** (25 mg/kg, ip.), (+)-**37** (40 mg/kg, ip.), (+)-**37** (25 mg/kg, ip.) combination Ator (30 mg/kg, po.), **21** (15 mg/kg), or gemcitabine (40 mg/kg, ip.) every 3 days. Tumor growth was measured through calipers, and tumor volumes and body weight were recorded. The calculation of tumor volumes was according to the formula 0.5 × length × width.[2] After 18 days, all mice were executed, and the tumors were finely excised for further study.

The pancreatic carcinoma PDX animal model was conducted according to the previously described procedures.[62] Briefly, human pancreatic specimens and the corresponding nontumor adjacent tissues were obtained from patients who had undergone a surgical pancreatic cancer excision. Fresh tumor tissues were sterilely incised into ∼3 mm^3 pieces and inoculated subcutaneously in the right flank of nude mice. The remaining tumor tissues were stored in liquid nitrogen. When the tumors have successfully engrafted, tumor samples were passaged into the third generation of nude mice for the following studies. After 12 days, the mice were allocated into three groups (n = 5) and received equal amounts of solvent (ip.), (+)-**37** (40 mg/kg, ip.), **21** (15 mg/kg), or gemcitabine (40 mg/kg, ip.) every 3 days. After 18 days, all mice were executed and the tumors were finely excised for further study. All experimental procedures were approved by the Shandong University Animal Care and Use Committee and conformed to the NIH Guide for the Care and Use of Laboratory Animals (National Academies Press, 2011). For human studies, the protocols were reviewed and approved by the Research Ethics Committee of Shandong University Qilu Hospital, and the patients were provided with written informed consent forms.

ASSOCIATED CONTENT

Supporting Information

The Supporting Information is available free of charge at https://pubs.acs.org/doi/10.1021/jacsau.3c00228.

Extended figures and tables, materals, experimental methods and structural characterization data (PDF)

The HPLC inspection (purity and *ee* values), mass and NMR spectra of compounds (PDF)

AUTHOR INFORMATION

Corresponding Author

Hongxiang Lou − *Department of Natural Products Chemistry, Key Laboratory of Natural Products & Chemical Biology, Ministry of Education, School of Pharmaceutical Sciences, Shandong University, Jinan 250012, China;* orcid.org/0000-0003-3300-1811; Email: louhongxiang@sdu.edu.cn

Authors

Yong Sun − *Department of Natural Products Chemistry, Key Laboratory of Natural Products & Chemical Biology, Ministry of Education, School of Pharmaceutical Sciences, Shandong University, Jinan 250012, China*

Hongbo Zheng − *Department of Natural Products Chemistry, Key Laboratory of Natural Products & Chemical Biology, Ministry of Education, School of Pharmaceutical Sciences, Shandong University, Jinan 250012, China;* orcid.org/0000-0001-5628-5277

Lilin Qian − *Department of Natural Products Chemistry, Key Laboratory of Natural Products & Chemical Biology, Ministry of Education, School of Pharmaceutical Sciences, Shandong University, Jinan 250012, China*

Yue Liu − *Department of Natural Products Chemistry, Key Laboratory of Natural Products & Chemical Biology, Ministry of Education, School of Pharmaceutical Sciences, Shandong University, Jinan 250012, China*

Deyu Zhu − *Department of Biochemistry and Molecular Biology, School of Basic Medical Sciences, Cheeloo College of Medicine, Shandong University, Jinan 250012, China*

Zejun Xu − *Department of Natural Products Chemistry, Key Laboratory of Natural Products & Chemical Biology, Ministry of Education, School of Pharmaceutical Sciences, Shandong University, Jinan 250012, China;* orcid.org/0000-0002-3885-0524

Wenqiang Chang − *Department of Natural Products Chemistry, Key Laboratory of Natural Products & Chemical Biology, Ministry of Education, School of Pharmaceutical Sciences, Shandong University, Jinan 250012, China*

Jianwei Xu − *Department of General Surgery, Qilu Hospital of Shandong University, Jinan 250012, China*

Lei Wang − *Department of General Surgery, Qilu Hospital of Shandong University, Jinan 250012, China*

Bin Sun − *National Glycoengineering Research Center, Shandong University, Jinan 250100, China*

Lichuan Gu − *State Key Laboratory of Microbial Technology, Shandong University, Qingdao 266237, China*

Huiqing Yuan − *Key Laboratory of Experimental Teratology of the Ministry of Education, Institute of Medical Sciences, The Second Hospital of Shandong University, Jinan 250013, China*

Complete contact information is available at: https://pubs.acs.org/10.1021/jacsau.3c00228

Author Contributions

[▽]Y.S. and H.Z. contributed equally to this work. The manuscript was written through contributions of all authors. All authors have given approval to the final version of the manuscript. CRediT: **Yong Sun** conceptualization, data curation, formal analysis, funding acquisition, investigation, methodology, project administration, resources, software, supervision, validation, visualization, writing-original draft, writing-review & editing; **Hongbo Zheng** conceptualization,

https://doi.org/10.1021/jacsau.3c00228
JACS Au 2023, 3, 2749−2762

data curation, formal analysis, funding acquisition, investigation, methodology, project administration, resources, software, supervision, validation, visualization, writing-original draft, writing-review & editing; **Hong-Xiang Lou** formal analysis, funding acquisition, project administration, resources, supervision, writing-original draft, writing-review & editing.

Notes

The authors declare no competing financial interest.

■ ACKNOWLEDGMENTS

This work was supported by the National Natural Science Foundation of China (nos. 81630093 and 81874293), the Foundation of Ministry of Science and Technology of the People's Republic of China (2019YFA0905701), the National Natural Science Foundation of China Young Scientist Fund (no. 82003586), and the Major Basic Research Program of Shandong Provincial Natural Science Foundation (ZR2019ZD26). We acknowledge Dr. Daniel A. Strassfeld for proofreading this article.

■ REFERENCES

(1) Conrad, M.; Angeli, J. P.; Vandenabeele, P.; Stockwell, B. R. Regulated Necrosis: Disease Relevance and Therapeutic Opportunities. *Nat. Rev. Drug Discovery* **2016**, *15*, 348−366.
(2) Ke, B.; Tian, M.; Li, J.; Liu, B.; He, G. Targeting Programmed Cell Death Using Small-Molecule Compounds to Improve Potential Cancer Therapy. *Med. Res. Rev.* **2016**, *36*, 983−1035.
(3) Yang, W. S.; SriRamaratnam, R.; Welsch, M. E.; Shimada, K.; Skouta, R.; Viswanathan, V. S.; Cheah, J. H.; Clemons, P. A.; Shamji, A. F.; Clish, C. B.; Brown, L. M.; Girotti, A. W.; Cornish, V. W.; Schreiber, S. L.; Stockwell, B. R. Regulation of Ferroptotic Cancer Cell Death by GPX4. *Cell* **2014**, *156*, 317−331.
(4) Zhang, C.; Liu, X.; Jin, S.; Chen, Y.; Guo, R. Ferroptosis in Cancer Therapy: A Novel Approach to Reversing Drug Resistance. *Mol. Cancer* **2022**, *21*, 1−12.
(5) Wang, Y.; Wen, X.; Zhang, N.; Wang, L.; Hao, D.; Jiang, X.; He, G. Small-Molecule Compounds Target Paraptosis to Improve Cancer Therapy. *Biomed. Pharmacother.* **2019**, *118*, No. 109203.
(6) Gong, Y.; Fan, Z.; Luo, G.; Yang, C.; Huang, Q.; Fan, K.; Cheng, H.; Jin, K.; Ni, Q.; Yu, X.; Liu, C. The Role of Necroptosis in Cancer Biology and Therapy. *Mol. Cancer* **2019**, *18*, 1−17.
(7) Elgendy, S. M.; Alyammahi, S. K.; Alhamad, D. W.; Abdin, S. M.; Omar, H. A. Ferroptosis: An Emerging Approach for Targeting Cancer Stem Cells and Drug Resistance. *Crit. Rev. Oncol. Hematol.* **2020**, *155*, No. 103095.
(8) Liu, X.; Xia, S.; Zhang, Z.; Wu, H.; Lieberman, J. Channelling Inflammation: Gasdermins in Physiology and Disease. *Nat. Rev. Drug Discovery* **2021**, *20*, 384−405.
(9) Du, T.; Gao, J.; Li, P.; Wang, Y.; Qi, Q.; Liu, X.; Li, J.; Wang, C.; Du, L. Pyroptosis, Metabolism, and Tumor Immune Microenvironment. *Clin. Transl. Med.* **2021**, *11*, No. e492.
(10) Lu, Y.; Sun, W.; Du, J.; Fan, J.; Peng, X. Immunophotodynamic Therapy (IPDT): Organic Photosensitizers and Their Application in Cancer Ablation. *JACS Au* **2023**, *3*, 682−699.
(11) Yan, G.; Elbadawi, M.; Efferth, T. Multiple Cell Death Modalities and Their Key Features. *World Acad. Sci. J.* **2020**, *2*, 39−48.
(12) Fontana, F.; Raimondi, M.; Marzagalli, M.; Di Domizio, A.; Limonta, P. The Emerging Role of Paraptosis in Tumor Cell Biology: Perspectives for Cancer Prevention and Therapy with Natural Compounds. *Biochim. Biophys. Acta Rev. Cancer.* **2020**, *1873*, No. 188338.
(13) Kim, E.; Lee, D. M.; Seo, M. J.; Lee, H. J.; Choi, K. S. Intracellular Ca^{2+} Imbalance Critically Contributes to Paraptosis. *Front. Cell Dev. Biol.* **2021**, *8*, 1703.
(14) Bury, M.; Girault, A.; Mégalizzi, V.; Spiegl-Kreinecker, S.; Mathieu, V.; Berger, W.; Evidente, A.; Kornienko, A.; Gailly, P.; Vandier, C.; Kiss, R. Ophiobolin A Induces Paraptosis-Like Cell Death in Human Glioblastoma Cells by Decreasing BKCa Channel Activity. *Cell Death Dis.* **2013**, *4*, No. e561.
(15) Tian, W.; Li, J.; Su, Z.; Lan, F.; Li, Z.; Liang, D.; Wang, C.; Li, D.; Hou, H. Novel Anthraquinone Compounds Induce Cancer Cell Death through paraptosis. *ACS Med. Chem, Lett.* **2019**, *10*, 732−736.
(16) Tardito, S.; Bassanetti, I.; Bignardi, C.; Elviri, L.; Tegoni, M.; Mucchino, C.; Bussolati, O.; Franchi-Gazzola, R.; Marchio, L. Copper Binding Agents Acting as Copper Ionophores Lead to Caspase Inhibition and Paraptotic Cell Death in Human Cancer Cells. *J. Am. Chem. Soc.* **2011**, *133*, 6235−6242.
(17) Palmeri, C. M.; Petiti, J. P.; del Valle Sosa, L.; Gutiérrez, S.; De Paul, A. L.; Mukdsi, J. H.; Torres, A. I. Bromocriptine Induces Parapoptosis as The Main Type of Cell Death Responsible for Experimental Pituitary Tumor Shrinkage. *Toxicol. Appl. Pharmacol.* **2009**, *240*, 55−65.
(18) Liu, X.; Tang, C.; Wen, G.; Zhong, C.; Yang, J.; Zhu, J.; Ma, C. The Mechanism and Pathways of Dopamine and Dopamine Agonists in Prolactinomas. *Front. Endocrinol.* **2019**, *9*, 768.
(19) Wasik, A.; Almestrand, S.; Wang, X.; Hultenby, K.; Dackland, Å.-L.; Andersson, P.; Kimby, E.; Christensson, B.; Sander, B. WIN55, 212−2 Induces Cytoplasmic Vacuolation in Apoptosis-Resistant MCL Cells. *Cell Death Dis.* **2011**, *2*, e225−e225.
(20) Kim, S. H.; Kang, J. G.; Kim, C. S.; Ihm, S.-H.; Choi, M. G.; Yoo, H. J.; Lee, S. J. The HSP70 Inhibitor VER155008 Induces Paraptosis Requiring *de novo* Protein Synthesis in Anaplastic Thyroid Carcinoma Cells. *Biochem. Biophys. Res. Commun.* **2014**, *454*, 36−41.
(21) Tardito, S.; Barilli, A.; Bassanetti, I.; Tegoni, M.; Bussolati, O.; Franchi-Gazzola, R.; Mucchino, C.; Marchiò, L. Copper-Dependent Cytotoxicity of 8-Hydroxyquinoline Derivatives Correlates with Their Hydrophobicity and Does Not Require Caspase Activation. *J. Med. Chem.* **2012**, *55*, 10448−10459.
(22) Zheng, H.; Dong, Y.; Li, L.; Sun, B.; Liu, L.; Yuan, H.; Lou, H. Novel Benzo[a]quinolizidine Analogs Induce Cancer Cell Death through Paraptosis and Apoptosis. *J. Med. Chem.* **2016**, *59*, 5063−5076.
(23) Zhang, C.-Y.; Gao, Y.; Zhu, R.-X.; Qiao, Y.-N.; Zhou, J.-C.; Zhang, J.-Z.; Li, Y.; Li, S.-W.; Fan, S.-H.; Lou, H.-X. Prenylated Bibenzyls from The Chinese Liverwort *Radula Constricta* and Their Mitochondria-Derived Paraptotic Cytotoxic Activities. *J. Nat. Prod.* **2019**, *82*, 1741−1751.
(24) Shi, X.; Zhang, T.; Lou, H.; Song, H.; Li, C.; Fan, P. Anticancer Effects of Honokiol via Mitochondrial Dysfunction are Strongly Enhanced by The Mitochondria-Targeting Carrier Berberine. *J. Med. Chem.* **2020**, *63*, 11786−11800.
(25) Sandoval, C. O.; Simmen, T. Rab Proteins of the Endoplasmic Reticulum: Functions and Interactors. *Biochem. Soc. Trans.* **2012**, *40*, 1426−1432.
(26) Stenmark, H. Rab GTPases as Coordinators of Vesicle Traffic. *Nat. Rev. Mol. Cell. Bio.* **2009**, *10*, 513−525.
(27) Jin, H.; Tang, Y.; Yang, L.; Peng, X.; Li, B.; Fan, Q.; Wei, S.; Yang, S.; Li, X.; Wu, B.; Huang, M.; Tang, S.; Liu, J.; Li, H. Rab GTPases: Central Coordinators of Membrane Trafficking in Cancer. *Front. Cell Dev. Biol.* **2021**, *9*, No. 648384.
(28) Hutagalung, A. H.; Novick, P. J. Role of Rab GTPases in Membrane Traffic and Cell Physiology. *Physiol. Rev.* **2011**, *91*, 119−149.
(29) Chen, T. W.; Yin, F. F.; Yuan, Y. M.; Guan, D. X.; Zhang, E.; Zhang, F. K.; Jiang, H.; Ma, N.; Wang, J. J.; Ni, Q. Z.; Qiu, L.; Feng, J.; Zhang, X. L.; Bao, Y.; Wang, K.; Cheng, S. Q.; Wang, X. F.; Wang, X.; Li, J. J.; Xie, D. CHML Promotes Liver Cancer Metastasis by Facilitating Rab14 Recycle. *Nat. Commun.* **2019**, *10*, 2510 DOI: 10.1038/s41467-019-10364-0.
(30) Thomas, J. D.; Zhang, Y. J.; Wei, Y. H.; Cho, J. H.; Morris, L. E.; Wang, H. Y.; Zheng, X. F. Rab1A is an mTORC1 Activator and a Colorectal Oncogene. *Cancer Cell* **2014**, *26*, 754−769.

(31) Stigter, E. A.; Guo, Z.; Bon, R. S.; Wu, Y. W.; Choidas, A.; Wolf, A.; Menninger, S.; Waldmann, H.; Blankenfeldt, W.; Goody, R. S. Development of Selective, Potent RabGGTase Inhibitors. *J. Med. Chem.* **2012**, *55*, 8330−8340.
(32) Spiegel, J.; Cromm, P. M.; Itzen, A.; Goody, R. S.; Grossmann, T. N.; Waldmann, H. Direct Targeting of Rab-GTPase-Effector Interactions. *Angew. Chem., Int. Ed. Engl.* **2014**, *53*, 2498−2503.
(33) Shah, M. Y.; Ferrajoli, A.; Sood, A. K.; Lopez-Berestein, G.; Calin, G. A. microRNA Therapeutics in Cancer - An Emerging Concept. *EBioMedicine* **2016**, *12*, 34−42.
(34) Yang, Y.; Hou, N.; Wang, X.; Wang, L.; Chang, S.; He, K.; Zhao, Z.; Zhao, X.; Song, T.; Huang, C. miR-15b-5p Induces Endoplasmic Reticulum Stress and Apoptosis in Human Hepatocellular Carcinoma, Both in Vitro and In Vivo, by Suppressing Rab1A. *Oncotarget* **2015**, *6*, 16227−16238.
(35) Tzeng, H.-T.; Wang, Y.-C. Rab-Mediated Vesicle Trafficking in Cancer. *J. Biomed. Sci.* **2016**, *23*, 1−7, DOI: 10.1186/s12929-016-0287-7.
(36) Brown, J. L.; Lawrence, M. M.; Borowik, A.; Oliver, L.; Peelor, F. F., 3rd; Van Remmen, H.; Miller, B. F. Tumor Burden Negatively Impacts Protein Turnover as a Proteostatic Process in Noncancerous Liver, Heart, and Muscle, but Not Brain. *Eur. J. Appl. Physiol.* **2021**, *131*, 72−82.
(37) Qin, X.; Wang, J.; Wang, X.; Liu, F.; Jiang, B.; Zhang, Y. Targeting Rabs as a Novel Therapeutic Strategy for Cancer Therapy. *Drug Discovery Today* **2017**, *22*, 1139−1147.
(38) Cichocki, B. A.; Khobragade, V.; Donzel, M.; Cotos, L.; Blandin, S.; Schaeffer-Reiss, C.; Cianferani, S.; Strub, J. M.; Elhabiri, M.; Davioud-Charvet, E. A Class of Valuable (Pro-)Activity-Based Protein Profiling Probes: Application to the Redox-Active Antiplasmodial Agent Plasmodione. *JACS Au* **2021**, *1*, 669−689.
(39) Becker, T.; Wiest, A.; Telek, A.; Bejko, D.; Hoffmann-Roder, A.; Kielkowski, P. Transforming Chemical Proteomics Enrichment into a High- Throughput Method Using an SP2E Workflow. *JACS Au* **2022**, *2*, 1712−1723.
(40) Sun, Y.; Qiao, Y.; Liu, Y.; Zhou, J.; Wang, X.; Zheng, H.; Xu, Z.; Zhang, J.; Zhou, Y.; Qian, L. *ent*-Kaurane Diterpenoids Induce Apoptosis and Ferroptosis through Targeting Redox Resetting to Overcome Cisplatin Resistance. *Redox. biol.* **2021**, *43*, No. 101977, DOI: 10.1016/j.redox.2021.101977.
(41) Kolb, H. C.; Finn, M. G.; Sharpless, K. B. Click Chemistry: Diverse Chemical Function from a Few Good Reactions. *Angew. Chem., Int. Ed. Engl.* **2001**, *40*, 2004−2021.
(42) Ong, S. E.; Mann, M. A Practical Recipe for Stable Isotope Labeling by Amino Acids in Cell Culture (SILAC). *Nat. Protoc.* **2006**, *1*, 2650−2660.
(43) Zhuang, S.; Li, Q.; Cai, L.; Wang, C.; Lei, X. Chemoproteomic Profiling of Bile Acid Interacting Proteins. *ACS Cent. Sci.* **2017**, *3*, 501−509.
(44) Chen, P.; Chaikuad, A.; Bamborough, P.; Bantscheff, M.; Bountra, C.; Chung, C. W.; Fedorov, O.; Grandi, P.; Jung, D.; Lesniak, R.; Lindon, M.; Müller, S.; Philpott, M.; Prinjha, R.; Rogers, C.; Selenski, C.; Tallant, C.; Werner, T.; Willson, T. M.; Knapp, S.; Drewry, D. H. Discovery and Characterization of GSK2801, a Selective Chemical Probe for the Bromodomains BAZ2A and BAZ2B. *J. Med. Chem.* **2016**, *59*, 1410−1424.
(45) Ignatev, A.; Kravchenko, S.; Rak, A.; Goody, R. S.; Pylypenko, O. A Structural Model of the GDP Dissociation Inhibitor Rab Membrane Extraction Mechanism. *J. Biol. Chem.* **2008**, *283*, 18377−18384.
(46) Pylypenko, O.; Rak, A.; Durek, T.; Kushnir, S.; Dursina, B. E.; Thomae, N. H.; Constantinescu, A. T.; Brunsveld, L.; Watzke, A.; Waldmann, H.; Goody, R. S.; Alexandrov, K. Structure of Doubly Prenylated YPT1: GDI Complex and the Mechanism of GDI-Mediated Rab Recycling. *EMBO J.* **2006**, *25*, 13−23.
(47) Seifert, T.; Malo, M.; Lengqvist, J.; Sihlbom, C.; Jarho, E. M.; Luthman, K. Identification of The Binding Site of Chroman-4-One-Based Sirtuin 2-Selective Inhibitors Using photoaffinity Labeling in Combination with Tandem Mass Spectrometry. *J. Med. Chem.* **2016**, *59*, 10794−10799.
(48) Jumper, J.; Evans, R.; Pritzel, A.; Green, T.; Figurnov, M.; Ronneberger, O.; Tunyasuvunakool, K.; Bates, R.; Žídek, A.; Potapenko, A. Highly Accurate Protein Structure Prediction with AlphaFold. *Nature* **2021**, 1−11, DOI: 10.1038/s41586-021-03819-2.
(49) Allan, B. B.; Moyer, B. D.; Balch, W. E. Rab1 Recruitment of p115 into a *cis*-SNARE Complex: Programming Budding COPII Vesicles for Fusion. *Science* **2000**, *289*, 444−448.
(50) You, K.; Wang, L.; Chou, C.-H.; Liu, K.; Nakata, T.; Jaiswal, A.; Yao, J.; Lefkovith, A.; Omar, A.; Perrigoue, J. G. QRICH1 Dictates The Outcome of ER Stress through Transcriptional Control of Proteostasis. *Science* **2021**, *371*, No. eabb6896, DOI: 10.1126/science.abb6896.
(51) Meng, K.; Zhuang, X.; Peng, T.; Hu, S.; Yang, J.; Wang, Z.; Fu, J.; Xue, J.; Pan, X.; Lv, J.; Liu, X.; Shao, F.; Li, S. Arginine GlcNAcylation of Rab small GTPases by the pathogen Salmonella typhimurium. *Commun. Biol.* **2020**, *3*, 287.
(52) Jurczyluk, J.; Munoz, M. A.; Skinner, O. P.; Chai, R. C.; Ali, N.; Palendira, U.; Quinn, J. M.; Preston, A.; Tangye, S. G.; Brown, A. J.; Argent, E.; Ziegler, J. B.; Mehr, S.; Rogers, M. J. Mevalonate Kinase Deficiency leads to Decreased Prenylation of Rab Gtpases. *Immunol. Cell Biol.* **2016**, *94*, 994−999.
(53) Lai, A. C.; Crews, C. M. Induced Protein Degradation: An Emerging Drug Discovery Paradigm. *Nat. Rev. Drug Discovery* **2017**, *16*, 101−114.
(54) Pylypenko, O.; Rak, A.; Durek, T.; Kushnir, S.; Dursina, B. E.; Thomae, N. H.; Constantinescu, A. T.; Brunsveld, L.; Watzke, A.; Waldmann, H.; Goody, R. S.; Alexandrov, K. Structure of Doubly Prenylated Ypt1: GDI Complex and The Mechanism of GDI-Mediated Rab Recycling. *EMBO J.* **2006**, *25*, 13−23.
(55) Ming, Z.; Guo, C.; Jiang, M.; Li, W.; Zhang, Y.; Fan, N.; Zhong, Y.; Meng, X.; Yang, S. Bioinformatics Analysis of Rab GDP Dissociation Inhibitor Beta and Its Expression in Non-Small Cell Lung Cancer. *Diagn. Pathol.* **2014**, *9*, 201.
(56) Sun, Z. L.; Zhu, Y.; Wang, F. Q.; Chen, R.; Peng, T.; Fan, Z. N.; Xu, Z. K.; Miao, Y. Serum Proteomic-Based Analysis of Pancreatic Carcinoma for The Identification of Potential Cancer Biomarkers. *Biomed. Pharmacother.* **2007**, *1774*, 764−771.
(57) Xu, D. D.; Xu, C. B.; Lam, H. M.; Wong, F. L.; Leung, A. W. N.; Leong, M. M. L.; Cho, W. C. S.; Hoeven, R.; Lv, Q.; Rong, R. Proteomic Analysis Reveals That Pheophorbide A-Mediated Photodynamic Treatment Inhibits Prostate Cancer Growth by Hampering GDP-GTP Exchange of Ras-Family Proteins. *Photodiagnosis Photodyn. Ther.* **2018**, *23*, 35−39.
(58) Lee, D. H.; Chung, K.; Song, J.-A.; Kim, T.-h.; Kang, H.; Huh, J. H.; Jung, S.-g.; Ko, J. J.; An, H. J. Proteomic identification of paclitaxel-resistance associated hnRNP A2 and GDI2 proteins in human ovarian cancer cells. *J. Proteome Res.* **2010**, *9*, 5668−5676.
(59) Tadros, S.; Shukla, S. K.; King, R. J.; Gunda, V.; Vernucci, E.; Abrego, J.; Chaika, N. V.; Yu, F.; Lazenby, A. J.; Berim, L. De novo lipid synthesis facilitates gemcitabine resistance through endoplasmic reticulum stress in pancreatic cancer. *Cancer Res.* **2017**, *77*, 5503−5517, DOI: 10.1158/0008-5472.CAN-16-3062.
(60) N'Guessan, K. F.; Davis, H. W.; Chu, Z.; Vallabhapurapu, S. D.; Lewis, C. S.; Franco, R. S.; Olowokure, O.; Ahmad, S. A.; Yeh, J. J.; Bogdanov, V. Y. Enhanced efficacy of combination of gemcitabine and phosphatidylserine-targeted nanovesicles against pancreatic cancer. *Mol. Ther.* **2020**, *28*, 1876−1886.
(61) Le Calvé, B.; Griveau, A.; Vindrieux, D.; Maréchal, R.; Wiel, C.; Svrcek, M.; Gout, J.; Azzi, L.; Payen, L.; Cros, J. Lysyl oxidase family activity promotes resistance of pancreatic ductal adenocarcinoma to chemotherapy by limiting the intratumoral anticancer drug distribution. *Oncotarget* **2016**, *7*, 32100 DOI: 10.18632/oncotarget.8527.
(62) Zhang, H.; Cohen, A. L.; Krishnakumar, S.; Wapnir, I. L.; Veeriah, S.; Deng, G.; Coram, M. A.; Piskun, C. M.; Longacre, T. A.; Herrler, M. Patient-derived xenografts of triple-negative breast cancer reproduce molecular features of patient tumors and respond to

mTOR inhibition. *Breast Cancer Res.* **2014**, *16*, 1−16, DOI: 10.1186/bcr3640.

https://doi.org/10.1021/jacsau.3c00228
JACS Au 2023, 3, 2749−2762